Composite Structures 140 (2016) 192–201

Contents lists available at ScienceDirect

Composite Structures

journal homepage: www.elsevier.com/locate/compstruct

Full-field strain measurements at the micro-scale in fiber-reinforced composites using digital image correlation

Mahoor Mehdikhani *, Mohammadali Aravand, Baris Sabuncuoglu, Michaël G. Callens, Stepan V. Lomov, Larissa Gorbatikh

KU Leuven, Department of Materials Engineering, Kasteelpark Arenberg 44, 3001 Leuven, Belgium

ARTICLE INFO

Article history:
Available online 30 December 2015

Keywords:
Digital image correlation (DIC)
Scanning electron microscopy (SEM)
Micro-mechanics
Polymer-matrix composites (PMCs)
Finite element analysis (FEA)

ABSTRACT

Few studies have been conducted to monitor inter-fiber deformations in fiber-reinforced composites. In the present work, we demonstrate full-field strain measurements in the composites at the micro-scale, using digital image correlation (DIC). The study is performed on a unidirectional glass fiber reinforced composite loaded in transverse three-point bending inside an environmental scanning electron microscope. A nano-scale random speckle pattern of high quality is created. Validity of the measured fields is assessed against results of a finite element (FE) model with boundary conditions retrieved from the experiment. A good agreement is found between the DIC-measured and FE-predicted results. The precise recognition of very small-scale strain concentrations requires enhancement of the correlation process and removal of microscopy imperfections. The investigated methodology shows promise for real-time deformation measurements in composites at the micro-scale.

1. Introduction

Digital image correlation (DIC) is an optical method to track changes in a series of deformed images. It is used to measure displacements and strains on the surface of a deforming material in a non-contact way. The correlation process uses the gray intensity pattern inside virtually created *subsets*. Hence, each subset should have a unique pattern, which, in the absence of an inherent surface texture, results from an artificial random speckle pattern on the surface of the material [1,2]. DIC has been widely applied to measure deformation in composites at the macro- and meso-scales [3–9]. To track deformations of individual fibers and inter-fiber deformation in the matrix, the length scale of this technique should be reduced to the micro-scale. The need for the micro-scale DIC (μDIC) is particularly important in the field of nano-engineered fiber-reinforced composites and composites with multiphase matrices where the effect of modifications is most pronounced at this scale [10–13].

A number of difficulties appear in the application of μDIC to different materials, and several studies have been conducted to progressively tackle them. Up to now, μDIC has been mostly applied to metals. It started with use of high-magnification optical microscopy in the late 90s to early 2000s, when baseline errors in displacement measurement, problems with the image contrast, refocus errors, and lens aberrations were the main difficulties [14,15]. Higher magnification DIC analyses were accomplished through engaging scanning electron microscopy (SEM) [16–18]. Challenges related to drift and spatial distortions, and SEM based noise were explored in [19–21]. Another challenge in μDIC is application of a suitable tracking pattern to the specimen surface [22]. μDIC was also applied to non-conductive materials in a few studies such as [23,24].

μDIC has been rarely applied to fiber-reinforced polymer-based composites. The promise of this technique for analysis of micro-scale deformations in these composites was first shown in [25], where Canal et al. analyzed the deformation in a unidirectional E-glass/epoxy composite under transverse compression. For a microscopic window at three different magnifications (250×, 2000×, and 6000×), they achieved fine displacement maps for the component in the loading direction. At high magnifications, the loading-direction strain maps showed lower accuracy in identifying the strain concentrations and exact location of fibers. The average composite strain in the microscopic window was derived with an error around 2.5%, but the quantitative values of strain average in each phase were not accurately obtained. The reason, pointed by the authors, was that the high deformation gradient at the fiber/matrix interface could not be captured. It was smoothed out because DIC calculates strains by taking the derivate of the displacements over a small strain window, not

* Corresponding author. Tel.: +32 16376925; fax: +32 16321990.
E-mail address: mahoor.mehdikhani@mtm.kuleuven.be (M. Mehdikhani).

http://dx.doi.org/10.1016/j.compstruct.2015.12.020
0263-8223/

differentiating between the two phases on which it is placed. That is why it is challenging to apply μDIC to heterogeneous microstructures with a high property mismatch in the constituents.

The present study continues the line of research established in [25], applying μDIC to fiber-reinforced composites. The methodology, in line with the one proposed in [25], is exerted on an example of a unidirectional glass fiber/epoxy composite to further investigate the measurement and interpretation issues. The specimen is loaded in transverse three-point bending, and a microscopic study zone on the tensile deformation region is monitored with an environmental scanning electron microscope (ESEM). Efforts are made to produce a nano-scale random speckle pattern, with quality assessed by analysis of DIC *measurement errors*. Other difficulties related to fitting the mechanical test set-up inside the ESEM chamber, the imaging distortions and noise, charging effect, and maintaining the field of view fixed under loading are looked at. The validity of the μDIC results is evaluated against a finite element analysis (FEA). Limitations of μDIC on fiber-reinforced composites, particularly concerning high local strains, are then discussed. The preliminary studies were conducted in [26].

The authors' longer term goal is to further apply this technique to study microscopic phenomena such as damage initiation and development in composites, and to provide a tool which allows evaluation of the changes in the mechanical behavior brought by introducing nano-reinforcements in the fiber-reinforced composite [27].

2. μDIC methodology

The investigated μDIC approach includes such steps as preparing specimens, applying a speckle pattern, assessing the pattern, deforming the material, capturing micrographs, appraising microscopy adequacy, optimizing DIC parameters, applying DIC, filtering out random noise, and validating DIC results against FE predictions.

2.1. Composite material

The studied material is a unidirectional glass/epoxy composite produced by vacuum infusion, previously studied in [28]. The glass fiber is *Advantex® Glass SE 1500 2400*, with an average diameter of 17 μm, and the epoxy matrix is *EPIKOTE™Resin MGS® LR 135 LV*, with *EPIKURE™Curing Agent MGS® LH 137* as hardener. The Young's moduli of the glass fiber and epoxy matrix are 81 GPa and 3 GPa, and the Poisson's ratios are 0.22 and 0.30, respectively. The average composite thickness is 1.9 mm and the average fiber volume fraction is 61.9%. The composite plate is cut into specimens of $68.0 \times 8.0 \times 1.9\ mm^3$ dimension in such a way that fibers are aligned in the width direction. The surfaces perpendicular to the fibers direction are grinded by SiC abrasive papers (320, 800, 1200, and 4000 grit, consecutively) and polished by a diamond slurry of 1-μm particle size, followed by an oxide polishing suspension.

2.2. Speckle pattern enhancement and DIC parameters

2.2.1. Speckle deposition

The electron microscopy image from the composite cross-section (Fig. 1a) reveals that the material does not possess a suitable texture in its natural state. The presence of large areas with similar gray intensity levels asks for an external random speckle pattern. The pattern is produced through deposition of a powder on the specimen surface. When choosing the appropriate powder, the following parameters were taken into account: the particle size, level of absorption and distribution on the surface, tendency to aggregate, and gray level contrast with composite surface. A sub-micron alumina powder (*TM-DAR* series of *TAIMICRON*) produced by *TAIMEI CHEMICALS Co., Ltd*. is selected for the study. The average size of the particles is 220 nm. To avoid particle aggregation, a dispersant for stabilizing alumina suspensions such as *DARVAN-CN* (a trademark of *R.T. Vanderbilt Holding Company, Inc.* for ammonium polymethacrylate) is used [29].

Several trials are done to achieve a suitable speckle pattern. First, a 1-wt.% suspension of alumina in distilled water is prepared, and a drop of it is applied to the polished surface of one of the specimens. Then, it is left in the ambient air to be dried. After gold sputtering, large aggregates can be observed all over the surface through electron microscopy (Fig. 1b). Aggregates could be formed before or during the deposition, causing a significant error in DIC by creating large areas with unvarying gray intensity level. Additionally, deformation of the aggregates can be different from the deformation of the underlying surface. In order to prevent particle aggregation ultrasonication along with magnetic stirring is applied to the suspension before deposition. A new polished specimen is speckled with this suspension. Fig. 1c shows that ultrasonication eliminates large aggregates. To remove small-scale aggregates and to further enhance the dispersion of nano-particles, *DARVAN-CN* is added to the suspension before ultrasonication. Fig. 1d, which is captured from the surface of a new specimen, speckled with the dispersant-including suspension, shows that the aggregation is drastically decreased.

The concentration of alumina is also optimized. In Fig. 1d, it is observed that 1 wt.% is quite high, which makes it difficult to observe the underlying surface. Thus, a 0.1-wt.% suspension is produced, taking advantage of both ultrasonication along with magnetic stirring and *DARVAN-CN*. The micrograph from the specimen speckled with the 0.1-wt.% suspension (Fig. 1e) displays that the distribution of particles is not uniform. To further enhance the distribution, the concentration is reduced to 0.05 wt.% (using ultrasonication, magnetic stirring, and *DARVAN-CN*), but the deposition process is performed twice. The second deposition is done once the first layer is dried. With this approach a well-dispersed and evenly distributed speckle pattern is achieved (Fig. 1f). The amount of *DARVAN-CN* in each suspension is 1/10 of the alumina weight. The surface of all speckled specimens in this study is coated with a thin conductive film in order to diminish the charging effect.

2.2.2. Assessment of the pattern quality

To examine the quality of the optimized speckle pattern (Fig. 1f) we used a so-called *strain deviation analysis*, where DIC is applied to virtually deformed images. For this, a micrograph with the resolution of 1424×968 pixel^2 ($125 \times 85\ \mu m^2$) is taken from the speckled surface as the study zone (Fig. 2b). The length of the micrograph is extended by 15 pixels, using the *lanczos3* resizing method in *MATLAB*. This virtual deformation is equivalent to a value of 0.0106 for the horizontal component of the Lagrangian strain. The virtual deformation is analyzed through DIC to assess the deviations from the applied strain. The same strain deviation analysis is also applied to a poorly-speckled specimen (Fig. 1e). For DIC, *VIC-2D 2009* software (*Correlated Solutions*) is used. The sizes of *subset*, *step*, and *smoothing filter* (described in 2.2.3 and [30]) for this strain deviation analysis, are set to 21 pixels, 1 pixel, and 5 data points, respectively. All of the DIC analyses in this study are performed with a *normalized squared differences* criterion, *optimized 4-tap* interpolation, and *Gaussian* subset weights. Lagrangian strains are computed from the resulting displacements and smoothed with a 90% center-weighted decay filter [30]. All strain values given in Sections 2.2.2, 2.2.3, and 2.3 refer to the horizontal component.

It is expected to obtain homogeneous strain maps if the deformation is applied uniformly. In reality, digital resizing of an image is not totally uniform all over the image, and local deformation

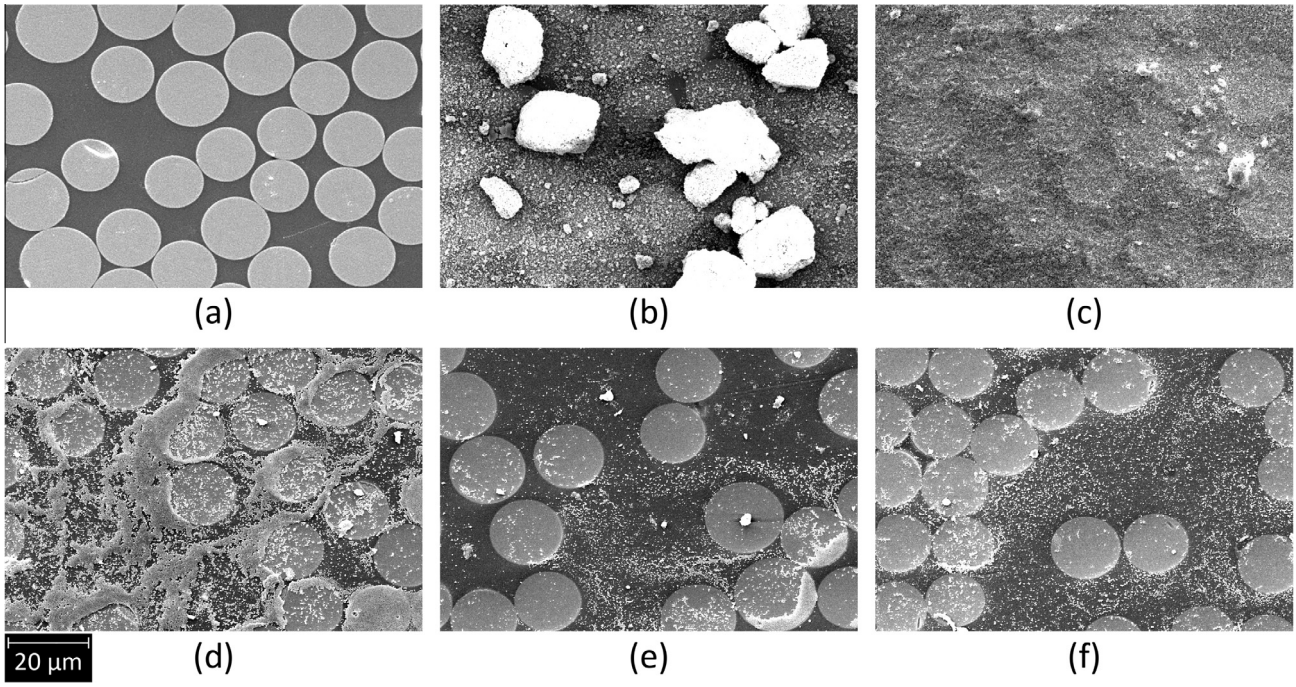

Fig. 1. SEM images of (a) a bare specimen surface and (b)–(f) speckled surfaces with alumina suspensions using (b) 1 wt.% alumina, without ultrasonication and stirring, without dispersant agent; (c) 1 wt.% alumina, with ultrasonication and stirring, without dispersant agent; (d) 1 wt.% alumina, with ultrasonication and stirring, with dispersant agent; (e) 0.1 wt.% alumina, with ultrasonication and stirring, with dispersant agent and (f) twice deposition of 0.05 wt.% suspension, with ultrasonication and stirring, with dispersant agent.

depends on the interpolation method used. This causes heterogeneity, similar to those studied in [31], in resulting strain fields. In order to reduce the interpolation effect on the heterogeneity in the initial resulting strain, the strain field, resulted from digital resizing, is estimated by averaging horizontal profiles of strain through the image width. This interpolation strain field is subtracted from the initial strain field, resulting in a strain deviation map, which exhibits measurement-arising non-uniformity. The strain deviation maps of poor and optimized patterns are shown in Fig. 2a and b. The mean strain, before subtraction, is accurately calculated (0.0106) for both patterns. However, the strain deviation map of the poorly-speckled specimen shows a higher level of non-uniformity, particularly in areas free of speckles. This non-uniformity of strain (in the case of uniform deformation) is the result of DIC errors, mainly, in imperfectly-speckled areas, referred to as *measurement error* in this study. This non-uniformity can be measured by means of standard deviation of strain calculation. The standard deviation for the poor pattern is 0.0031, while it is 0.0013 for the optimized pattern. The lower level of strain deviations for the optimized pattern is also evident by comparing strain deviations along an arbitrary chosen straight line (Fig. 2c), displayed on both maps.

2.2.3. Evaluation of DIC parameters

The strain deviation analysis is also used to evaluate the suitable size for subset, step, and smoothing filter. For this, similarly, a micrograph from the well-speckled surface is virtually deformed using the *lanczos3* resizing method in *MATLAB*. The deformation, which is a 15-pixel extension in the length, is analyzed through eight DIC analyses with different sets of subset, step, and filter sizes. The same procedure for decreasing the interpolation heterogeneity effect, as explained above, is performed. The resulting mean strain and standard deviation (as a measure for strain non-uniformity) for each analysis (corresponding to one set of parameters) are given in Table 1. It reveals that the average strains over the study zone are precisely calculated through DIC against the applied (virtual) strain, i.e. 0.0106. It also shows that increase in the subset size decreases the strain standard deviation. This is because larger subsets hold more speckles and can be distinguished more precisely [2]. However, this increase reduces the resolution of the correlation [32], and hence local variations may not be accurately detected in the analysis of real deformation. In fact, the optimum subset size should be a compromise between small values, which provide more detailed measurements, but also higher measurement error, and large values, which decrease the error. The investigated subsets are drawn on the study zone micrograph in Fig. 2b, and as can be seen, no area as small as the subsets, can be found without speckles inside. Considering the fact that the subset has to be large enough to contain a sufficiently distinctive pattern all over the image, the 61-pixel subset ensures the higher accuracy of DIC with this speckle pattern.

Similarly, reduction in the step size increases the standard deviation of the measured strain. Step size defines the spacing of the points that are analyzed in DIC [30]. Thus, with a lower step size, more pixels are analyzed and a more detailed correlation is possible, identifying more imperfectly-speckled areas as well. According to [32] the highest resolution with the lowest strain noise can be achieved by minimizing the step size and using a moderate subset. The standard deviations related to the step size of 2 pixels is still far below the mean strain. It is acceptable to lose a small amount of accuracy to acquire strain maps with higher resolution. Therefore, the step size of 2 pixels is selected for further analysis. The trade-off scenario also applies to the filter size selection. Especially for inhomogeneous deformation, a proper size should be carefully selected. Smoothing filter reduces the noise in the resulting strain. Small filters result in better spatial resolution and detection of strain concentrations, but more noise in strain [2]. To get a balance between accuracy and strain smoothness, the 15 data points filter is selected. The optimum values for the subset, step, and filter size resulted from this analysis are 61 pixels (5.35 μm), 2 pixels

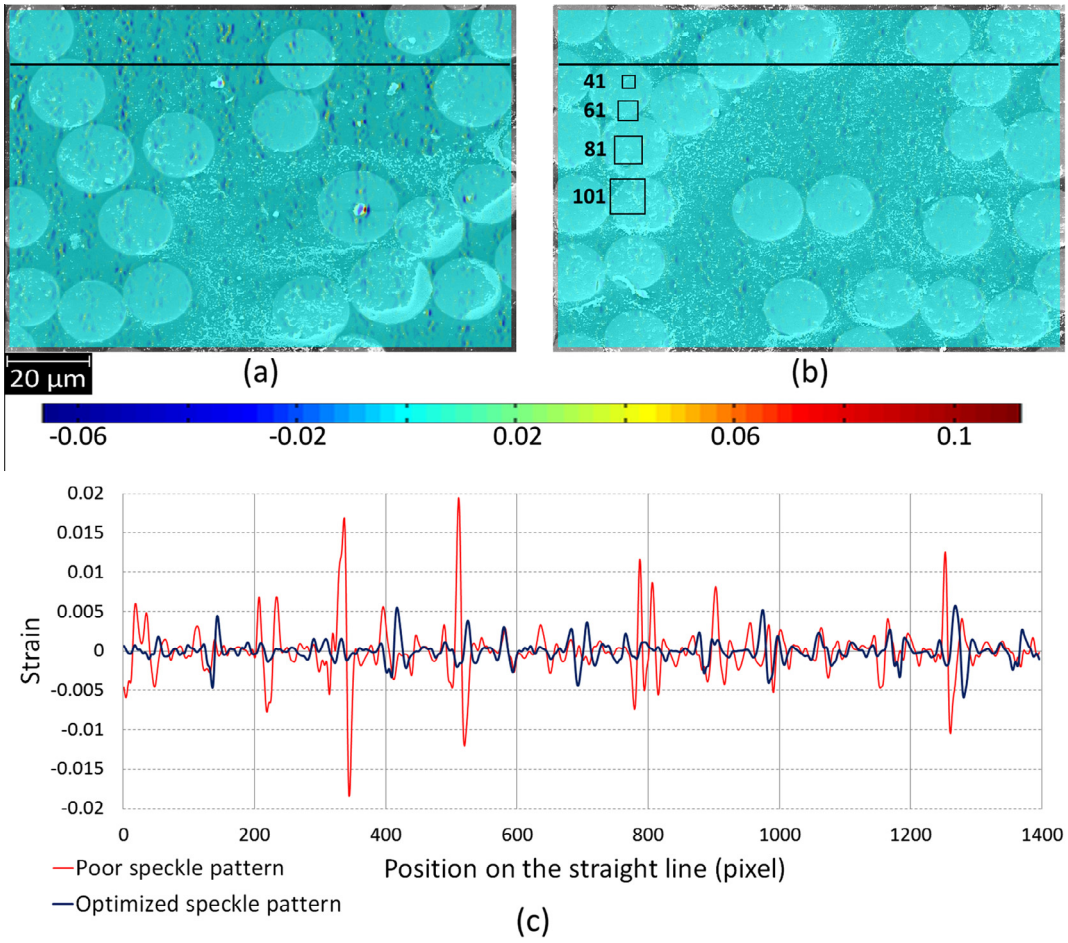

Fig. 2. Strain deviation analysis: effect of the quality of speckle pattern on the accuracy of DIC strain deviation maps for a (a) poor and (b) optimized speckle pattern, (c) comparison of the strain deviation along the straight line shown on the two strain maps in (a) and (b).

Table 1
Strain deviation analysis: effect of DIC parameters on the resulting horizontal strain from virtual deformation on the well-speckled image. The applied strain is 0.0106.

Subset size (pixel)	Step size (pixel)	Filter size (data point)	Mean strain	Strain standard deviation
41	5	15	0.0106	0.000070
61	5	15	0.0106	0.000054
81	5	15	0.0106	0.000041
101	5	15	0.0106	0.000034
61	10	15	0.0106	0.000017
61	**2**	**15**	**0.0106**	**0.000134**
61	1	15	0.0106	0.000194
61	2	25	0.0106	0.000097
61	2	5	0.0106	0.000180

Note: the parameters in bold were chosen for further calculations.

(0.17 μm), and 15 data points (2.63 μm), respectively. In the resulting DIC strain map of strain deviation analysis with these optimum parameters, the maximum local deviation, from the virtual strain of 0.0106, is 0.0008.

2.3. Image acquisition in in-situ tests

After a suitable speckle pattern is produced and optimum DIC parameters are selected from the strain deviation analysis, the specimen is prepared for the *in-situ* deformation. The deformation is provided by a transverse three-point bending experiment inside an ESEM chamber (*FEI/Philips XL30 ESEM FEG*). For this, a mini-tester stage (*Deben UK Limited*) is installed inside the ESEM. The specimen is placed on the bending stage such that the fibers are transversely aligned to the loading. Carbon tape is used to establish conductivity between specimen surface and the stage for reducing the charging effect. A study zone on the surface of the specimen is identified on a region just above the middle of the tensile edge (Fig. 3), so that the deformation is the maximum and the horizontal rigid body motion of the study zone is the minimum, which makes it easier to track the study zone during loading. Before the specimen is loaded, four micrographs are captured from the fixed study zone (still rigid body), in 30-s intervals to check the quality of the microscopy. They are analyzed through DIC, with the optimum values for the parameters. If several micrographs, without applying any deformations, are taken from a fixed field of view, DIC should ideally measure zero strain.

Nevertheless, deviations from zero are found in all strain component maps in each of the still-rigid-body micrographs. For the horizontal component, the resulting mean strain is between 0.0003 and 0.0005, and the standard deviation is between 0.0013 and 0.0033. Although measurement error might have a minor contribution in these spurious strains, they have more significant causes such as imaging distortions and noise [19–21], and/or charging effect. Therefore, these resulting false strains should be considered as the *microscopy error*. The highest false strains are observed on fibers, which can be due to occurrence of a considerable degree of charging effect on them. Though the false strains on

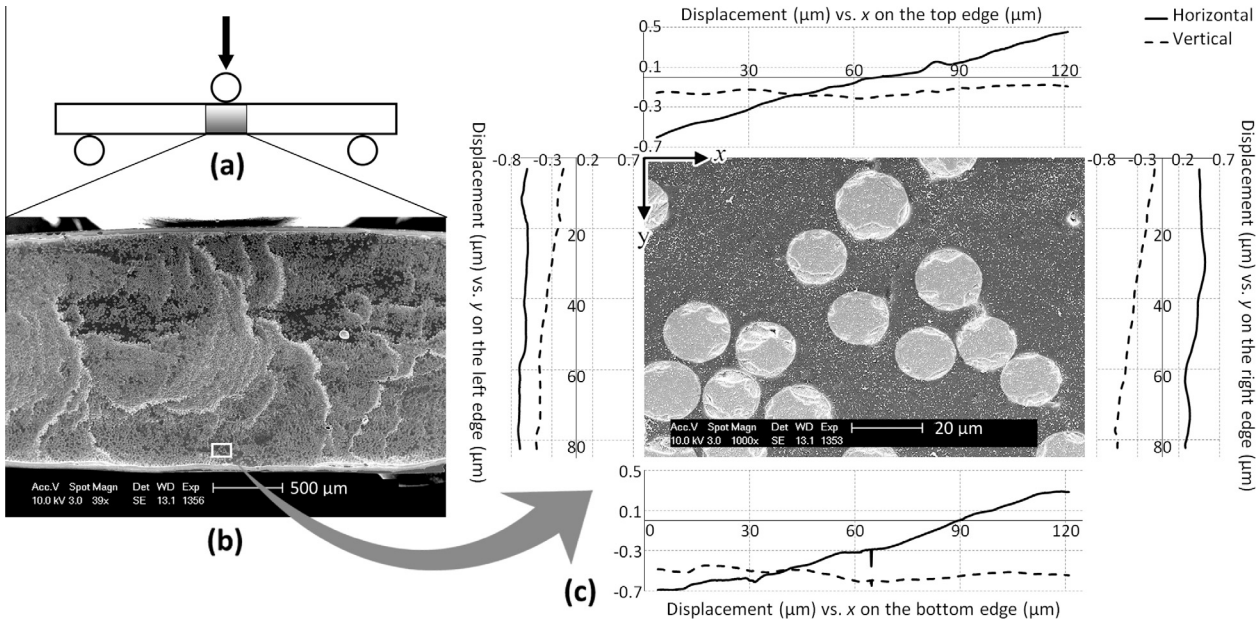

Fig. 3. The study zone chosen for strain mapping, shown (a) schematically on the specimen in three-point bending, (b) on the specimen cross-section, (c) at the working magnification (1000×), with the DIC-measured displacements profiles on each edge. The value and sign of displacements are reported with respect to the coordinate axes shown on the top left corner of (c).

fibers hold a high level of magnitude, the absolute value of local false strains in the matrix never exceeds 0.0050. The significance of the microscopy error as well as the measurement error will be assessed after the DIC analysis of the real deformation is carried out and the order of magnitude for the mean and local factual strains is determined.

After rigid body imaging, the specimen is loaded in three-point bending using a 50-N load cell and a speed of 0.1 mm/min. The mini-tester is stopped every 30 s to adjust the field of view on the study zone by repositioning the bending stage, and capture a micrograph with the resolution of 1424×968 pixel^2 (125×85 µm^2 at a magnification of 1000×, 1 pixel = 0.0877 µm). A secondary electron (SE) detector is used, the voltage and spot size are 10.0 kV and 3.0, respectively, and the working distance (WD) is 13.1 mm. In each stop, finding the study zone and capturing a micrograph take around 40 s and relaxation in force in this time interval is below 0.05 N. The three-point bending is performed with 59 consecutive stops and with 60 micrographs taken. The final stop corresponds to the applied force of nearly 26 N, and the bending deflection of 1.7 mm.

DIC is performed on the 60 micrographs of the deformation with the optimized parameter values stated in Section 2.2.3. A 1401×957 pixel^2 rectangle is selected inside the study zone as the area of interest and the maps are displayed on a 1340×896 pixel^2 (118×79 µm^2) area (e.g. Fig. 4a). DIC calculates the mean strain to be 0.0091 for the last (59th) step. This strain level is close to the value of the (virtual) strain of 0.0106 applied for investigating the DIC parameters; therefore, the performed virtual deformation is an appropriate simulation for the real deformation in the study zone. Consequently, the resulting strain deviation in the strain deviation analysis with the optimized parameters can be considered as estimation for the measurement errors in the real-deformation analysis. The standard deviation was 0.0001 and the maximum local deviation was 0.0008 (Section 2.2.3). The microscopy-arising errors also affect the correlation results. As it was explored above, the maximum values for the mean of the spurious strains, occurring mostly on fibers, and the standard deviation were 0.0005 and 0.0033, respectively, and the absolute value of local false strains in the matrix region was below 0.0050. The maximum local strain in the real-deformation DIC map is 0.0240 (see Section 3.2). Hence, the errors from measurement and microscopy will not be very significant, except on fibers, the deformation in which is not of interest in this study. Furthermore, the possible errors from out-of-plane motion can be neglected in the presence of these measurement and microscopy errors.

2.4. Finite element model

In order to validate the results of the µDIC, they are compared with finite element (FE) predictions. The latter are performed in the commercial FEA package ABAQUS, based on the real microstructure examined in the experiment. The geometry and distribution of fibers are determined by a *MATLAB* circle detection code, which receives the micrograph of the study zone as input, and exports center coordinates and radii of all the fibers, to be then read in ABAQUS. The geometry of the cut fibers on the micrograph edges is manually implemented into the model. Assuming no out-of-plane deformation, the FE model is set up as a two-dimensional problem under plane strain assumptions. Before meshing, the matrix edges and fibers interfaces are seeded such that the elements around the fibers inside the matrix are three times finer than the elements on the matrix edges. The elastic mechanical properties of the fibers and matrix are assigned according to the data provided in Section 2.1. The boundary conditions (BCs) must accurately simulate the real loading on the study zone. The best source for this information is DIC results; therefore, BCs are derived from the experimental data. A *Python* script is developed to match a data point in the DIC displacement matrix with a node on the edges of the model, and assign the displacements of the data point to that node. Thus, the BCs of all the edge nodes can be defined to simulate the loading of the last step of the deformation. The DIC-resulting displacements (in which the rigid body displacement of the study zone is largely compensated) on the edges of the study zone are depicted on each edge in Fig. 3c.

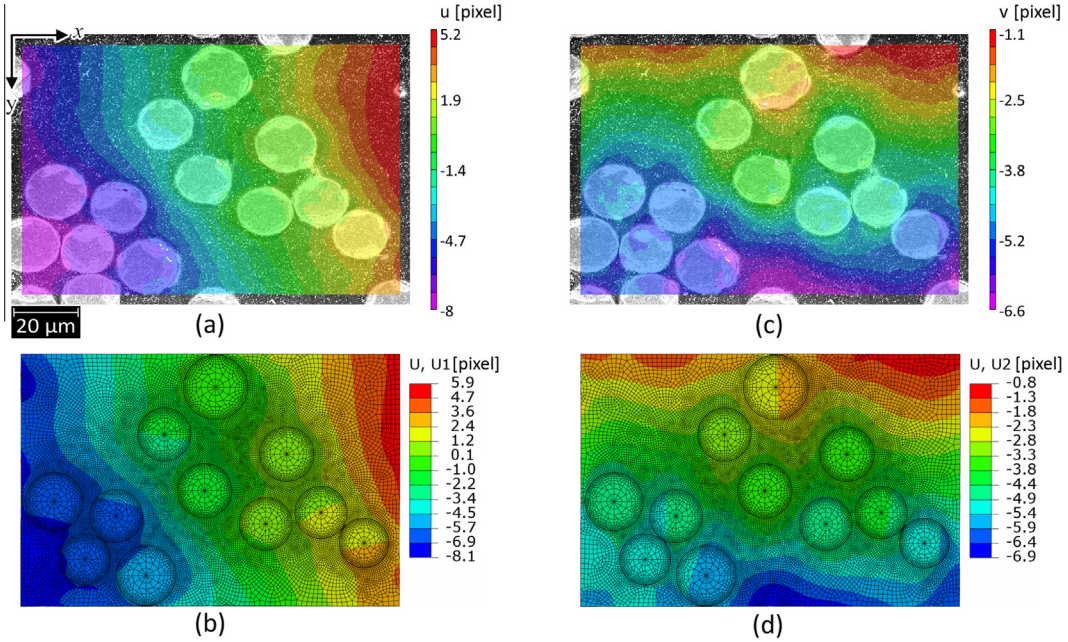

Fig. 4. Horizontal displacement maps resulted from (a) DIC and (b) FEA and vertical displacement maps resulted from (c) DIC and (d) FEA.

3. Results and discussion

From now on, results from both methods, DIC and FEA, are reported for the last (59th) step of the deformation unless otherwise is specified. The origin of the coordinate system in FEA is placed at the same position as DIC (top left corner) with the same axes directions to allow comparison between the maps (shown on Figs. 3c, 4a, 5a).

It should be noted that the rigid body displacement is largely compensated by locating the study zone in each deformation step, before image acquisition. Thus, the DIC displacement results correspond mainly to deformation of the study zone. The displacement profiles, shown in Fig. 3, reflect heterogeneity of the material. They exhibit general features, which could be expected from the displacement near a tensile side of a bend beam: for example, similar horizontal displacements on the top and bottom edges of the study zone. However, because of the heterogeneity and asymmetry of the study zone, some features, which would be expected in a homogeneous beam, are not present, notably non-zero horizontal displacement in the middle of the bottom edge of the study zone. The asymmetry of the displacements corresponds to the asymmetry of the microstructure with concentration of stiff fibers near the left side of the bottom edge of the study zone. Furthermore, a small deviation of the location of the study zone from the exact middle of the specimen, which is highly probable at the micro-scale, contributes to the asymmetry of horizontal displacement along the top and bottom edges.

3.1. Displacement analysis

Fig. 4a and b displays horizontal displacement maps (excluding most of the rigid body displacement of the study zone), measured experimentally using DIC and predicted by FEA, respectively. The maps are in a good level of agreement. The absolute horizontal displacement grows toward the side edges of the study zone. Additionally, the fibers in a cluster at the bottom left corner tend to move together. Similarly, the vertical displacement maps for DIC and FEA are in good agreement (Fig. 4c and d). An increase (in absolute value) toward the specimen bottom edge can be observed in both maps. Both methods could also detect that the displacement fronts are distorted by the presence of fibers. Based on the difference in the variation range of the maps, one can conclude that DIC correctly recognizes that higher displacement occurs in the horizontal direction than in the vertical one. It needs to be noted that the vertical displacements would have been much larger than the horizontal ones if the rigid body displacement of the study zone (bending deflection) had been added.

3.2. Strain analysis

The horizontal and vertical mean strains, calculated from DIC data, are 0.0091 and −0.0049, and from FEA analysis, are 0.0090 and −0.0049, respectively, which is expected, as the boundary displacement conditions for FEA are derived from DIC measurements. The full-filed strain analysis through the μDIC methodology, as it was discussed in Section 2.3, suffers measurement and microscopy errors, which appear as noises in the results. Assuming a linear response of the study zone in the elastic region, a technique to filter out the random noises is applying time (or average applied strain)-dependent linear regression of the strain values at each point of resulting strain fields, and accepting the result of the regression as the filtered strain values. This smoothing technique is proposed and described in [4]. All of the DIC-resulting strains in this study, from now on, are reported after applying the linear regression filtering. A few time steps were identified as outliers through the filtering and they are excluded from the analysis. The influence of the filtering procedure on the correct representation of the strain map features (like strain concentrations) and an illustration of the time-dependent strain regression is discussed at end of this section.

Fig. 5a and c respectively represents e_{xx} and e_{yy} components of DIC-resulting strain. The strain maps demonstrate that the DIC analysis could isolate the fiber strain from the matrix strain. This is expected as the elastic deformation of fibers is much smaller than that of the matrix. However, some spurious high strain concentrations can be observed inside fibers. With these spurious strains, some small regions on fibers appear to be under compression in the horizontal direction, and under tension in the vertical

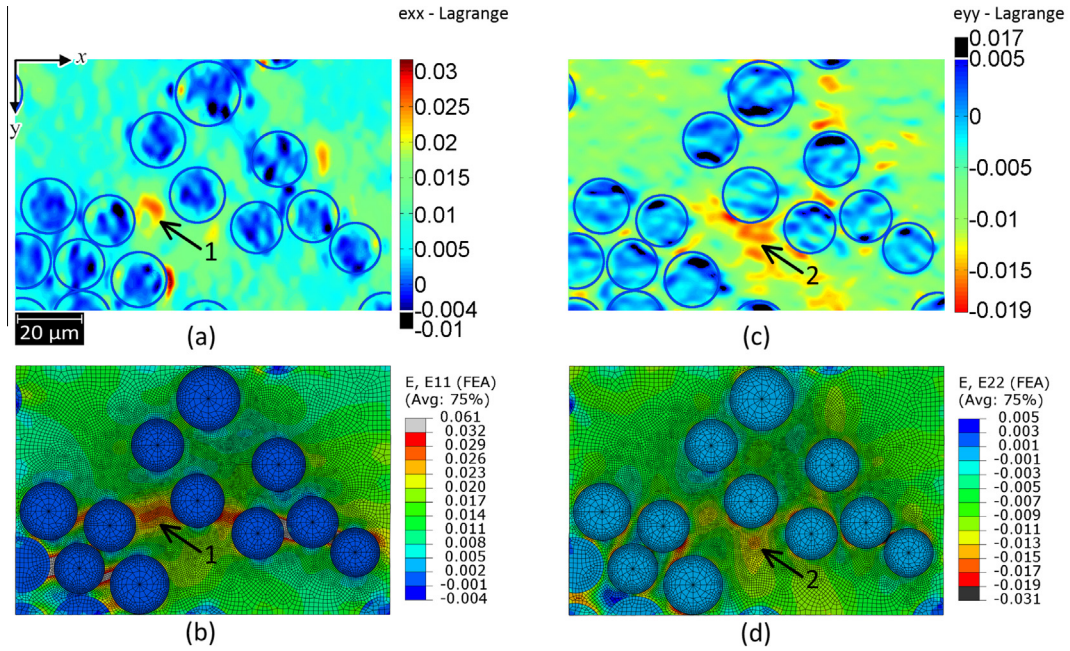

Fig. 5. Strain maps measured by DIC (a: horizontal, c: vertical) and predicted by FEA (b: horizontal, d: vertical). Numbered arrows show the similarly detected strain concentrations.

direction. This, as discussed in Section 2.3, is a microscopy artifact, resulting from high charging effect occurring on fibers, which can distort the DIC results. In order to diminish the significance of these spurious strains, the lower limit of the color legend in e_{xx} strain map is increased to −0.0040, and the upper limit of the color legend in e_{yy} strain map is reduced to 0.0050 (according to the FEA strain maps, Fig. 5b and d). Consequently, the spurious strains fall out of the ranges.

The e_{xx} map (Fig. 5a) holds larger difference in strain fields of fibers and matrix than e_{yy} (Fig. 5c). The absolute value of local strains is also higher in the e_{xx} map. This is because the examined area is mainly loaded in the *x*-direction. This leads to higher deformation of the matrix in the *x*-direction than in the *y*-direction. In combination with a very small deformation in the fibers, this creates a larger difference between e_{xx} strains in the fibers and matrix. The higher deformation in the *x*-direction can be concluded from the mean strain values as well. The e_{xx} map also reveals illustrative data about the mode of loading. As it is clear in Fig. 5a, the strain is positive almost all over the matrix, meaning that DIC could accurately recognize the tensile loading in the *x*-direction, on the study zone. On the other hand, values of e_{yy} (Fig. 5c) are mainly negative in the matrix, thus indicating compression in the *y*-direction. This confirms that µDIC could correctly assess the Poisson's effect and validate that the area is, in general, expanding in the *x*-direction and shrinking in the *y*-direction. The edges of the fibers are not exactly identified through the strain fields, particularly for e_{xx} (Fig. 5a). In addition to the false strains on fibers, the reason can be displacement averaging over subsets [33] and/or strain smoothing over filters in DIC. Taking into account these operations, DIC has a difficulty to detect small-scale strain concentrations as well as strains at the interface between phases with high mismatch in elastic properties [25].

Now, the DIC-measured strain maps are compared with FEA-predicted maps. In order to allow this comparison, the upper legend limit of the horizontal strain map and the lower legend limit of the vertical strain map, resulting from FEA, are restricted to those from the DIC data in Fig. 5. The values that fall outside this range are colored in gray and black for highest positive and negative strains, respectively. The difference in the legend range, as discussed in the previous paragraph, is mostly because DIC could hardly detect small-scale strain concentrations, particularly in between touching fibers. These strain concentrations would not have been captured either if elements in the FE model had been much larger.

The FEA strain maps (Fig. 5b and d) confirm most of the observations in the DIC maps. As can be noticed in Fig. 5b, the *x*-direction strain is high between adjacent fibers, nearly aligned in the *x*-direction, and the highest between almost-touching fibers that correlates to what is called the *shortest interfiber distance in the loading direction* in [34]. Comparing the *x*-direction strain maps from DIC and FEA (Fig. 5a and b), both have detected a strain concentration region (*Arrow 1*) between two adjacent fibers in the *x*-direction. It seems that the other strain concentration areas between adjacent fibers, visible in Fig. 5b, could not be identified by DIC due to the small areas they occupy. Moreover, the strain map of FEA looks more uniform in each phase than that of DIC. This, as was explained, relates mainly to microscopy errors. Similarly, in *y*-direction strain maps from both DIC and FEA (Fig. 5c and d), fibers are well recognized as blue features with almost no deformation. The e_{yy} strain map from DIC (Fig. 5c) could distinguish most of the strain concentrations detected by FEA map (Fig. 5d), even in between very close fibers. One of them is pointed on both maps (*Arrow 2*) as an example.

Although in ideal tension conditions, no shear strain is expected, at a microscopic window of a heterogeneous material, local shear strains may appear. The shear maps from DIC and FEA of a small window in the study zone are illustrated in Fig. 6a and b. Both maps show nearly no strain for the fibers. The strain concentrations, captured by FEA, are nicely identified by DIC as well. The difference in the maps is the magnitude of the local strains. It seems that DIC could find the location of high-level concentrations, but has problems in measuring their exact value. This also might be due to the strain smoothing.

Fig. 7b and e shows profiles of e_{xx} and e_{yy} along a 65-µm path, named *a*, shown on the corresponding maps (Fig. 7a and d). Comparing with FEA strain profiles along the same path, DIC could

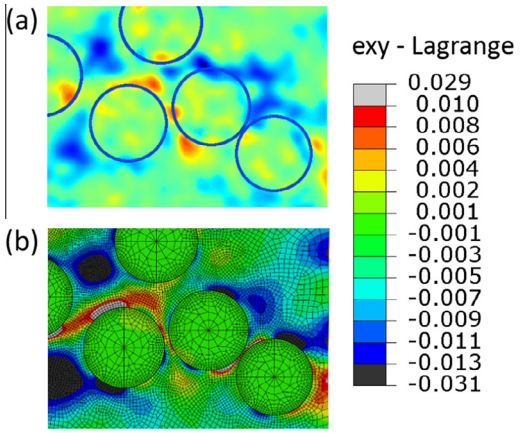

Fig. 6. Shear strain maps in the study zone, measured by (a) DIC and predicted by (b) FEA.

estimate the high strain in the matrix and distinguish the intersecting fiber on the path. This analysis is carried out for another path, named *b*, which goes across the strain maps and intersects five fibers, some of them almost touching (Fig. 7a and d). It can be observed that both horizontal and vertical strain profiles could detect all of the fibers, holding strains close to zero. The strain along the same section is also predicted by FEA. The DIC plots are in a general agreement with the FEA plot, and show μDIC ability in identifying features as small as few microns. However, a few differences are observed between DIC and FEA plots. Some of the fiber/matrix interfaces could not be accurately distinguished by DIC, especially in horizontal strain. Furthermore, the small-scale strain concentrations measured by DIC are not as high as those predicted by FEA. These two differences, as was already discussed, are a consequence of the displacement averaging and strain smoothing. The other difference is the noise in the strain, in particular on the fibers, which is mostly resulted from microscopy imperfections, as explained earlier.

In order to explore the validity of the strain measurements for a detected feature in the strain maps, the change of local strain in that feature against average strain in the study zone can be plotted. The average strain for each step is calculated through linearly fitting the measured average strains of all the 59 steps. Assuming elastic deformation, if the local strain is (almost) linearly increased, the feature is correctly detected. On the other hand, if the change in strain is random, the measurement noise is significant on that feature. This analysis is performed for horizontal strain at different locations, displayed in Fig. 7a, and the plots are shown in Fig. 8. It is clear that the point with moderate local strain in the matrix (*Point 1*) and the point in the strain concentration (*Point 2*) have a valid (linear) strain history, while the measurement for the point on the fiber (*Point 3*) are greatly violated by analysis error. The

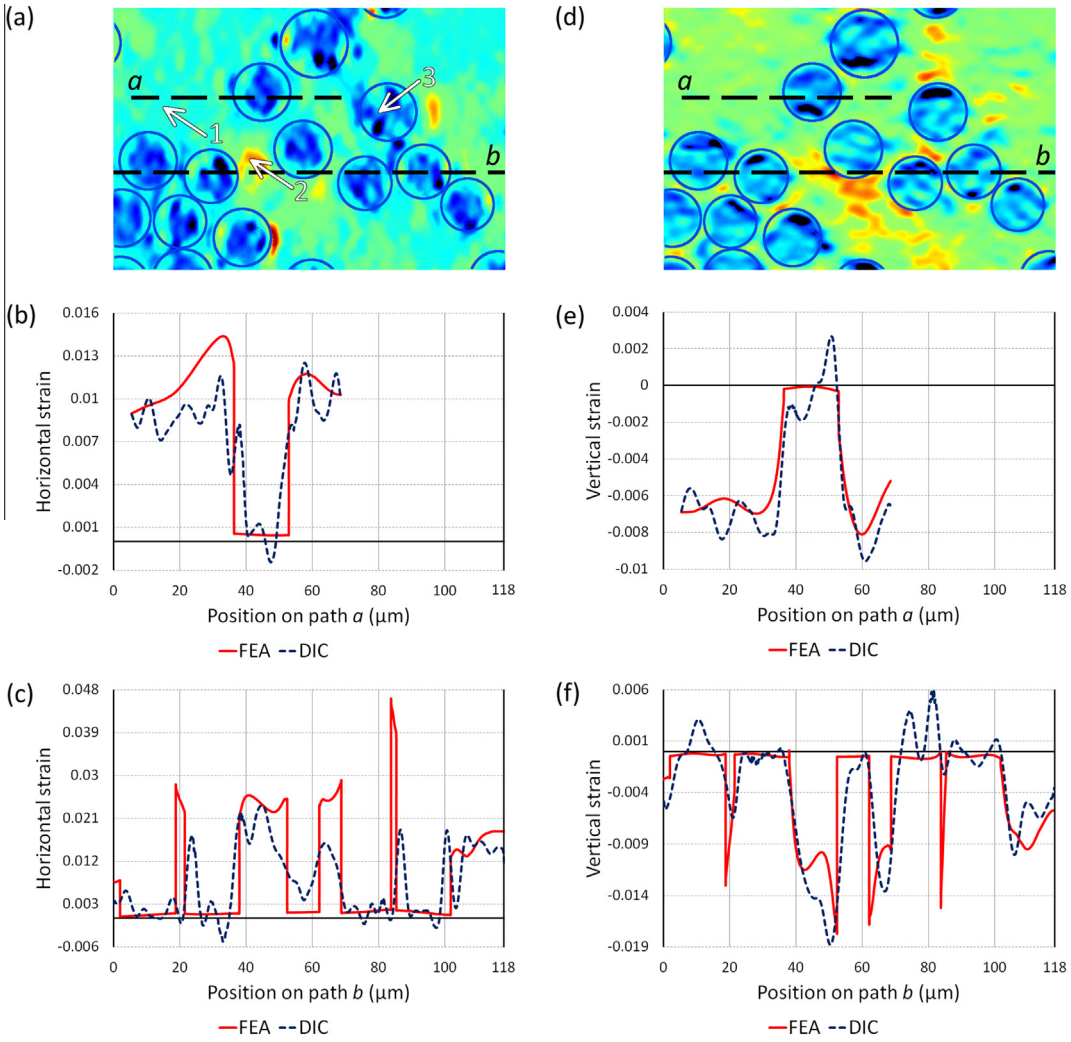

Fig. 7. Horizontal (a–c) and vertical (d–f) strain maps and strains along paths *a* and *b* (shown on the corresponding strain maps) measured by DIC and predicted by FEA.

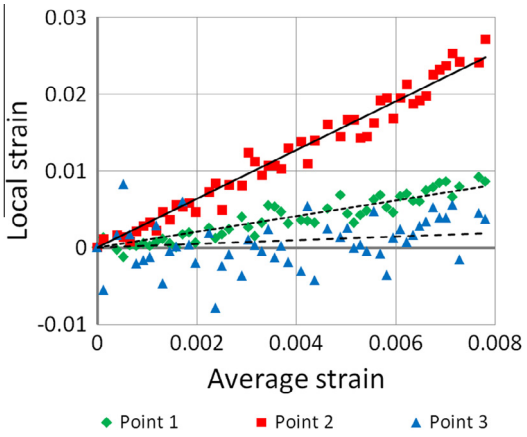

Fig. 8. Horizontal local strain in different locations (indicated in Fig. 7a by arrows) with different strain histories.

coefficient of determination values (R squared) for the linear fitting of local strains in *Point 1*, *Point 2*, and *Point 3* are 0.8702, 0.9688, and 0.0767, respectively. The very low R squared value for *Point 3* confirms that the high local strains measured on fibers are artifacts. The slope of the regression line can be negative for an analogous point with high microscopy error on the fibers, resulting in a negative horizontal strain in the filtered strain map for that point. Moreover, the comparison of the values for *Point 1* and *Point 2* indicates that analysis errors become less significant for matrix areas with higher local strains. It can be concluded that the analysis of the local strain history of each point seems to be a simple, but efficient technique for assessing the validity of DIC-resulting strains.

4. Conclusions

Micro-scale strain maps of a deforming composite, using digital image correlation, are investigated. The quality of the nano-scale speckle pattern is found to influence the accuracy of μDIC results. Areas free of speckles lead to larger errors in the correlation process. The speckle pattern and μDIC parameters are successfully optimized. For validity assessment of the μDIC results, anticipated errors, arising from correlation process and microscopy imperfections are evaluated. The random noise in resulting strain is reduced using a linear regression filter. Furthermore, by means of the regression analysis of local strain history of each point, a straightforward technique for evaluating the reliability of DIC results in the elastic regime is presented. Comparison with predicted displacement and strain results reveals a good agreement between μDIC and FEA maps. μDIC could detect strain concentrations even in between closely located fibers. However, due to averaging and smoothing in DIC, it has difficulty in measuring small-scale concentrations. The difficulty exists also in identifying areas of sudden changes in strain, e.g. fiber/matrix interfaces.

In order to achieve more accurate strain maps, further improvements are needed. Firstly, efforts are needed to reduce the effect of microscopy artifacts in consecutive micrographs. Secondly, a DIC algorithm, optimized for analysis of heterogeneous materials, will greatly help. In general, the μDIC methodology in this study showed a potential for real-time micro-scale analysis of deformation in fiber-reinforced composites.

Acknowledgments

The work was performed in the framework of the GOA/10/004 project (New model-based concepts for nano-engineered polymer composites) funded by the Research Council of KU Leuven. We would also like to thank Amir Ghodrati for his assistance in image processing analyses.

References

[1] Sutton MA, Orteu J-J, Schreier H. Image Correlation for Shape, Motion and Deformation Measurements: Basic Concepts, Theory and Applications. Springer Publishing Company, Incorporated; 2009.
[2] Pan B, Qian KM, Xie HM, Asundi A. Two-dimensional digital image correlation for in-plane displacement and strain measurement: a review. Meas Sci Technol 2009;20(6) 062001 (17pp).
[3] Lomov SV, Boisse P, Deluycker E, Morestin F, Vanclooster K, Vandepitte D, et al. Full-field strain measurements in textile deformability studies. Compos Part A Appl Sci Manuf 2008;39(8):1232–44.
[4] Lomov SV, Ivanov DS, Verpoest I, Zako M, Kurashiki T, Nakai H, et al. Full-field strain measurements for validation of meso-FE analysis of textile composites. Compos Part A Appl Sci Manuf 2008;39(8):1218–31.
[5] Totry E, Gonzalez C, Llorca J, Molina-Aldareguia JM. Mechanisms of shear deformation in fiber-reinforced polymers: experiments and simulations. Int J Fract 2009;158(2):197–209.
[6] Torres Arellano M, Crouzeix L, Douchin B, Collombet F, Hernández Moreno H, González Velázquez J. Strain field measurement of filament-wound composites at ±55° using digital image correlation: an approach for unit cells employing flat specimens. Compos Struct 2010;92(10):2457–64.
[7] Scalici T, Fiore V, Orlando G, Valenza A. A DIC-based study of flexural behaviour of roving/mat/roving pultruded composites. Compos Struct 2015;131:82–9.
[8] Montesano J, Selezneva M, Levesque M, Fawaz Z. Modeling fatigue damage evolution in polymer matrix composite structures and validation using in-situ digital image correlation. Compos Struct 2015;125:354–61.
[9] Gong W, Chen J, Patterson EA. An experimental study of the behaviour of delaminations in composite panels subjected to bending. Compos Struct 2015;123:9–18.
[10] De Greef N, Gorbatikh L, Lomov SV, Verpoest I. Damage development in woven carbon fiber/epoxy composites modified with carbon nanotubes under tension in the bias direction. Compos Part A Appl Sci Manuf 2011;42(11):1635–44.
[11] Romanov VS, Lomov SV, Verpoest I, Gorbatikh L. Can carbon nanotubes grown on fibers fundamentally change stress distribution in a composite? Compos Part A Appl Sci Manuf 2014;63:32–4.
[12] Romanov VS, Lomov SV, Verpoest I, Gorbatikh L. Modelling evidence of stress concentration mitigation at the micro-scale in polymer composites by the addition of carbon nanotubes. Carbon 2015;82:184–94.
[13] Aravand M, Lomov SV, Gorbatikh L. Morphology and fracture behavior of POM modified epoxy matrices and their carbon fiber composites. Compos Sci Technol 2015;110:8–16.
[14] Sun ZL, Lyons JS, McNeill SR. Measuring microscopic deformations with digital image correlation. Opt Laser Eng 1997;27(4):409–28.
[15] Chen J, Xia G, Zhou K, Xia G, Qin Y. Two-step digital image correlation for micro-region measurement. Opt Laser Eng 2005;43(8):836–46.
[16] Sabate N, Vogel D, Gollhardt A, Keller J, Cane C, Gracia I, et al. Residual stress measurement on a MEMS structure with high-spatial resolution. J Microelectromech Syst 2007;16(2):365–72.
[17] Jin H, Lu WY, Korellis J. Micro-scale deformation measurement using the digital image correlation technique and scanning electron microscope imaging. J Strain Anal Eng 2008;43(8):719–28.
[18] Lagattu F, Bridier F, Villechalse P, Brillaud J. In-plane strain measurements on a microscopic scale by coupling digital image correlation and an in situ SEM technique. Mater Charact 2006;56(1):10–8.
[19] Sutton MA, Li N, Joy DC, Reynolds AP, Li X. Scanning electron microscopy for quantitative small and large deformation measurements part i: SEM imaging at magnifications from 200 to 10,000. Exp Mech 2007;47(6):775–87.
[20] Sutton MA, Li N, Garcia D, Cornille N, Orteu JJ, McNeill SR, et al. Scanning electron microscopy for quantitative small and large deformation measurements – part II: experimental validation for magnifications from 200 to 10,000. Exp Mech 2007;47(6):789–804.
[21] Kammers AD, Daly S. Digital image correlation under scanning electron microscopy: methodology and validation. Exp Mech 2013;53(9):1743–61.
[22] Kammers AD, Daly S. Small-scale patterning methods for digital image correlation under scanning electron microscopy. Meas Sci Technol 2011;22(12) 125501 (12pp).
[23] Berfield TA, Patel JK, Shimmin RG, Braun PV, Lambros J, Sottos NR. Micro- and nanoscale deformation measurement of surface and internal planes via digital image correlation. Exp Mech 2007;47(1):51–62.
[24] Teixeira Pinto JM, Touchard F, Castagnet S, Nadot-Martin C, Mellier D. DIC strain measurements at the micro-scale in a semi-crystalline polymer. Exp Mech 2013;53(8):1311–21.
[25] Canal LP, Gonzalez C, Molina-Aldareguia JM, Segurado J, Llorca J. Application of digital image correlation at the microscale in fiber-reinforced composites. Compos Part A Appl Sci Manuf 2012;43(10):1630–8.
[26] Mehdikhani M, Aravand M, Sabuncuoglu B, Callens MG, Lomov SV, Gorbatikh L. Digital image correlation and finite element analysis applied to fiber-reinforced composites at the micro-scale. In: Digital image correlation 2,

Proceedings of the 20th international conference on composite materials (ICCM/20), Copenhagen; 19–24 July 2015. p. 4315–3.
[27] Romanov V, Lomov SV, Verpoest I, Gorbatikh L. Inter-fiber stresses in composites with carbon nanotube grafted and coated fibers. Compos Sci Technol 2015;114:79–86.
[28] Vallons K, Adolphs G, Lucas P, Lomov SV, Verpoest I. The influence of the stitching pattern on the internal geometry, quasi-static and fatigue mechanical properties of glass fibre non-crimp fabric composites. Compos Part A Appl Sci Manuf 2014;56:272–9.
[29] Briscoe BJ, Khan AU, Luckham PF. Optimising the dispersion on an alumina suspension using commercial polyvalent electrolyte dispersants. J Eur Ceram Soc 1998;18(14):2141–7.
[30] Vic-2D Reference Manual; 2009, Correlated Solutions: <www.correlatedsolutions.com>.
[31] Schreier HW, Braasch JR, Sutton MA. Systematic errors in digital image correlation caused by intensity interpolation. Opt Eng 2000;39(11):2915–21.
[32] Carter JW, Uchic M, Mills M. Impact of speckle pattern parameters on DIC strain resolution calculated from in-situ SEM experiments. In: Carroll J, Daly S, editors. Fracture, fatigue, failure, and damage evolution, vol. 5. Springer International Publishing; 2015. p. 119–26.
[33] Wang Y, Cuitiño AM. Full-field measurements of heterogeneous deformation patterns on polymeric foams using digital image correlation. Int J Solids Struct 2002;39(13–14):3777–96.
[34] Hojo M, Mizuno M, Hobbiebrunken T, Adachi T, Tanaka M, Ha SK. Effect of fiber array irregularities on microscopic interfacial normal stress states of transversely loaded UD-CFRP from viewpoint of failure initiation. Compos Sci Technol 2009;69(11–12):1726–34.